The Coordination Chemistry of Carbon Nanotubes: a Density Functional Study through a Cluster Model Approach

3 AUTHORS, INCLUDING:

Francesca Nunzi

Università degli Studi di Perugia

20 PUBLICATIONS   **261** CITATIONS

SEE PROFILE

The Coordination Chemistry of Carbon Nanotubes: a Density Functional Study through a Cluster Model Approach

Francesca Nunzi, Francesco Mercuri, and Antonio Sgamellotti*

Dipartimento di Chimica e Istituto di Scienze e Tecnologie Molecolari ISTM CNR, Università di Perugia, 1-06123 Perugia, Italy

Nazzareno Re

Facoltà di Farmacia, Università G. D'Annunzio, 1-66100 Chieti, Italy

Polycyclic aromatic hydrocarbons (PAHs) have been employed as models to investigate the functionalization of SWNTs sidewalls with transition metal complexes at the NL-DFT level, pointing out the most favorable coordination sites and the electronic properties of the resulting system. Molecular fragments topologically resembling the honeycomb lattice have been chosen, i.e., the pyrene ($C_{16}H_{10}$) and the coronene ($C_{24}H_{12}$) to respectively investigate an η^2 interaction on the C—C bond and an η^6 interaction on the hexagonal ring with suitable transition metal complexes. To reproduce the curvature of both (n,0) and (n,n) SWNTs surface, constrained geometry optimizations have been performed on these systems. Both geometrical parameters and bonding energies for the $(PH_3)_2M(C_{16}H_{10})$ (M = Ni, Pt) complexes suggest that η^2 bonding of metal fragments to nanotubes is much weaker than to fullerene, making questionable the stability of η^2 $M(PH_3)_2$ complexes of carbon nanotubes. The η^2 metal interaction with (9,0) and (5,5) bent-constrained pyrene models do not show any dependence on the (n,m) chiral vector. The analysis of the $Cr(CO)_3(C_{24}H_{12})$ complexes shows that the (9,0) and (5,5) bent-constrained coronenes, modeling carbon nanotubes, enforce the chromium atom to arrange an η^2 or η^4 coordination on the hexagonal ring, rather than an η^6 coordination, that is more favorable for the planar aromatic systems of benzene and planar coronene, modeling graphene sheets.

1. Introduction

Single-wall carbon nanotubes (SWNTs)[1] have induced great research interest because of their unusual physical, chemical, and mechanical properties.[2−5] These unique characteristics make them ideal candidates as building blocks of molecular scale machines and nanoelectronic devices. Understanding the chemistry of SWNTs is a viable route to developing controlled synthesis methods, enhance their solubility, and make them more amenable for the assembling of nanostructure precursors. The functionalization of the sidewalls with transition metal atoms, metal surfaces, or metal compounds provides new prospects in the manipulation of the electronic and magnetic properties of carbon nanotubes. The metal coordination represents an essential tool in organometallic crystal engineering, because it allows us to manipulate the functionalized systems and to modify the properties of the ligands by varying the nature of the metal and co-ligands, the coordination geometry, and the oxidation states.[6] The difficulties in obtaining pure SWNTs and in dissolving them in solvents make the chemical modification of SWNTs sidewalls a relatively unexplored area of research. SWNTs have been fluorinated,[7] and subsequently, fluorine atoms have been displaced with alkanes.[8] Chen et al. reported the derivatization of SWNTs dissolved in organic solutions with thionyl chloride and octadecylamine, as well as with chlorine through the use of dichlorocarbene.[9] Moreover, SWNTs have been ultrasonicated in a monochlorobenzene solution of poly(methyl methacry-
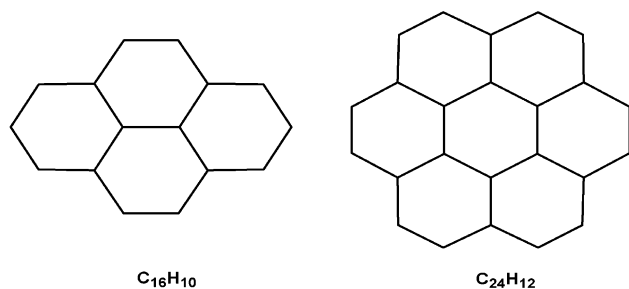
late),[10] and they have been noncovalently functionalized using a bifunctional molecule to form amide bonds for protein immobilization.[11]

However, not very much has been adressed in the area of the coordination of SWNTs with transition metals. Only recently, Banerjee and Wong accomplished the synthesis of functionalized carbon nanotubes by reaction with a transition metal complex, *trans*-IrCl(CO)(PPh$_3$)$_2$.[12] Spectroscopical analysis suggests that the iridium atom is coordinated to carbon nanotubes in an η^2 fashion, analogously to electron-deficient alkenes, whereas oxidized nanotubes allow the metal coordination through the oxygen atoms coating the sidewalls. Another interesting topic is the addition of Cr(CO)$_3$ metal complexes to the six-membered rings of SWNTs.[13] Among the inspected transition metal interactions with π systems,[14,15] (η^6-arene)tricarbonyl-chromium complexes have been extensively studied,[16−18] discovering a wide range of applications, such as chiral building blocks in total synthesis and their involvement in ligand design for asymmetric catalysis.[19−24] Indeed, it has been shown that the complexation with Cr(CO)$_3$ significantly modifies the structure and the reactivity of the complexed arenes.[25,26] Although Wilson[13] attempted the reaction of Cr(CO)$_6$ with SWNTs, pointing out the formation of an adduct "SWNT−Cr(CO)$_3$", experimental difficulties in the manipulation of the nanotubes made ineffective the characterization of the reaction product.

A detailed theoretical account for the interactions between transition metal complexes and carbon nanotubes is currently lacking, representing a challenging task for the theoretical

* To whom correspondence should be addressed. E-mail: sgam@thch.unipg.it. Phone: +39 075 5855516. Fax: +39 075 5855606.

Coordination Chemistry of Carbon Nanotubes

J. Phys. Chem. B, Vol. 106, No. 41, 2002 **10623**

SCHEME 1

$C_{16}H_{10}$ $C_{24}H_{12}$

chemists, because the electronic characteristics of SWNTs are very different from those of the parent systems, i.e., the graphite and the fullerene. Although the reactivity of nanotubes sidewalls has been compared to that of the basal plane of graphene,[27] the quasi-one-dimensionality of SWNTs makes their chemistry significantly different from that of the two-dimensional graphene sheet and zero-dimensional C_{60}. Even if nanotubes and graphite share the same honeycomb lattice, the curved carbon surface of SWNTs involves a rehybridization of carbon bonding orbitals (nonplanar sp^2 configuration).[28,29] C_{60} is a closed cage molecule, where the carbon atoms are arranged on a curved surface according to five- and six-membered rings. Consequently, the carbon bonding orbitals have more sp^3 character, which makes C_{60} generally more reactive than SWNTs.

Our aim is to investigate from a theoretical point of view the functionalization of carbon nanotubes with transition metal complexes, pointing out the most favorable coordination sites on the sidewalls and the electronic properties of the resulting system. Our study has been carried out on polycyclic aromatic hydrocarbons (PAHs) molecules as models of the whole SWNT. This strategy allows us to characterize the metal−ligand interaction through the analysis of the optimized geometries and electronic structures at an accurate level of theory (gradient corrected DFT). Moreover, clusters complexes containing PAHs and transition metals have stimulated growing research interest, because of their intriguing structure and bonding properties and several mass spectroscopy experiments have been performed on these species, to shed some light on their structural features, bonding properties and reactivity.[30−36] In this report, we focus on the possibility of an η^2 interaction on the C−C bond and an η^6 interaction on the six-membered ring of SWNTs with transition metal complexes. Following the pattern successfully adopted for fullerene models,[37] we identify molecular fragments topologically resembling the honeycomb lattice, that suit well for the description of such interactions, i.e., a pyrene fragment ($C_{16}H_{10}$) and a coronene fragment ($C_{24}H_{12}$) respectively for the η^2 and the η^6 bond fashion, see Scheme 1. Because such fragments are planar molecules made of hexagonal rings, suitable geometric constraints have been imposed to reproduce the curvature of the SWNTs surface. As stated above, the reliability of the molecular model approach has been successfully tested for the transition metal complexes of the fullerene,[37] where a bent-constrained pyracylene fragment ($C_{14}H_8$) has been found a good model for C_{60}.[38] Thus, useful information about the differences on the reactivity between fullerenes and carbon nanotubes toward transition metal complexes can be derived comparing the results on the basis of these molecular model clusters. Taking into account that both fullerenes and nanotubes show trivalent carbon atoms arranged on a curved surface, the main difference on the reactivity could be ascribed to the presence of cyclopentadienyl rings. The analysis through planar and bent-constrained models allows us to compare the interaction of transition metal complexes with the rolled-up

honeycomb lattice of SWNTs with respect to the planar graphene sheets. The success of pyracylene as a model for the whole C_{60} relies on the localized nature of the metal−ligand interaction, and it proves that the electronic picture of this interaction is not significantly affected by edge effects.[37] This paper intends to verify the reliability and the limits of the molecular model approach in investigating the interaction between transition metal complexes and carbon nanotubes. Taking into account the analysis derived from the cluster model approach, further investigations on the SWNTs complexation with transition metal complexes will be developed, by means of band structure calculations applying the framework of the density functional theory and periodic boundary conditions.

2. Computational Details

The calculations reported in this paper are based on the ADF (Amsterdam Density Functional) program package.[39] Its main features are the use of a density fitting procedure to obtain accurate Coulomb and exchange potentials in each SCF cycle, the accurate and efficient numerical integration of the effective one-electron Hamiltonian matrix elements, and the possibility to freeze core orbitals. The molecular orbitals are expanded using Slater-type orbitals (STO) basis set. We performed our calculations using two different basis sets. The first set, hereafter set I, consists of a double-ζ STO basis set for C (2s, 2p), P (3s, 3p), and H (is) atoms, whereas a double-ζ STO basis set for ns and np and a triple-ζ STO basis set for nd and $(n + 1)$s has been used for the transition metal atoms ($n = 3$ for Ni and Cr, $n = 5$ for Pt). As polarization functions, we used one $(n + 1)$p function for transition metals, one 3d for C and O, one 4d for P, and one 2p for H. The second basis set, hereafter called set II, differs from set I for the use of a triple-ζ STO basis set for C, P, and H. All of the geometry optimizations have been performed using the basis set I, because ligand basis of double-ζ quality plus polarization functions can accurately describe the geometries for organometallics systems, as outlined in refs 37 and 40. Bonding energy calculations were carried out with basis set I for nickel and chromium complexes, because the use of a larger ligand basis set does not affect significantly the computed values, provided that corrections for basis set superposition errors (BSSE) have been included. On the other hand, bonding energy estimates for platinum complexes require the use of basis set II, as shown in ref 37.

The LDA exchange correlation potential and energy were used, within the framework of the Vosko−Wilk−Nusair parametrization,[41] for homogeneous electron gas correlation, including the Becke's nonlocal correction,[42] to the local exchange expression and the Perdew's nonlocal correction[43] to the local expression of correlation energy.

Because the relativistic effects play an important role in describing the electronic structure and relative energetics of the species containing a heavy metal, such as platinum, they were taken into account by the Pauli formalism, the Pauli Hamiltonian including first-order scalar relativistic corrections (Darwin and mass-velocity) while neglecting spin−orbit corrections.[44,45]

Using the fragment-oriented approach implemented in the ADF program, the bond dissociation energy D(M−L) between the ligand L and the metal fragment M has been calculated according to eq 1:

$$D(M - L) = E^*(M - L) + BSSE + E_M^R + E_L^R =$$
$$E(M - L) + E_M^R + E_L^R \quad (1)$$

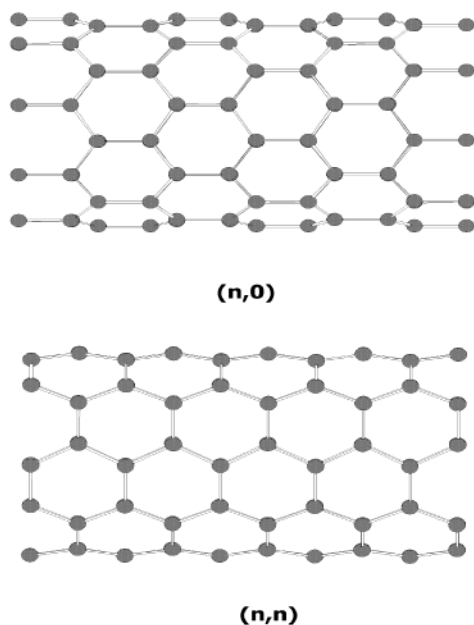We first evaluated the "snapping energies", $E^*(M - L)$, i.e.,

Figure 1. Structures of (*n*,0) and (*n*,*n*) carbon nanotubes.

the energy required to snap the metal−ligand bond into non-reorganized fragments, and then we computed the energies E_M^R and E_L^R) corresponding to the relaxation energies of the two fragments. We also calculated the basis set superposition error (BSSE), by applying the counterpoise method.[46] Corrections for zero-point vibration were not included because they are expected to give small contributions.

The bond dissociation energy is further decomposed into three contributions:

$$D(M - L) = -[E_{prep} + E_{ster} + E_{orb}] \qquad (2)$$

The first term, E_{prep}, is the preparation energy and represents the energy necessary to convert the fragments from their equilibrium geometries to the conformation they assume in the optimized structure of the overall complex. Because the fragments have been considered in the same closed shell state both in the complex formation and as free molecules, this term corresponds simply to the sum of the fragments relaxation energies, $E_M^R + E_L^R$. E_{ster} represents the steric repulsion between the two fragments and consists of two components, E_{elstat} and E_{pauli}. The first, E_{elstat}, is the electrostatic interaction of the nuclear charges and the unmodified electronic charge density of one fragment with those of the other fragment. The second component, E_{pauli}, is the so-called Pauli repulsion, which is essentially due to the antisymmetry requirement on the total wave function. E_{orb}, known as orbital interaction term, represents the attracting orbital interactions which give rise to the energy lowering upon coordination. This term can be further decomposed into contributions from the distinct irreducible representations Γ of the whole system, according to the extended transition state method.[45b]

3. Results

The electronic structure and, hence, the physical and chemical properties of nanotubes stronlgy depend on the (*n*,*m*) chiral vector. Carbon nanotubes are usually classified depending on the orientation of the hexagons in the honeycomb lattice with respect to the main axis of the tube, giving rise to two limit structures, the (*n*,0) zigzag and the (*n*,*n*) armchair (see Figure 1). In our molecular fragment approach, the considered molec-

TABLE 1: Optimized Geometries of Planar and Bent-Constrained Pyrene Models[a]

$C_{16}H_{10}$	d_t	δ	C−C(I)	C−C(II)	E_σ[b]
planar	∞	0	1.420 (1.430)[c]	1.425 (1.425)[c]	0
(17,0)	13.3	7.2	1.426	1.420	0.5
(12,0)	9.4	12.8	1.426	1.418	1.0
(9,0)	7.0	18.7	1.419	1.418	2.1
(5,0)	3.9	31.8	1.431	1.439	7.5
(10,10)	13.6	9.6	1.419	1.429	0.5
(7,7)	9.5	14.4	1.416	1.428	1.0
(5,5)	6.8	21.4	1.422	1.428	2.3
(3,3)	4.0	34.8	1.439	1.438	6.6

[a] Bond lengths are given in angstroms, bond angles are given in degrees, and energy values are given in eV; C−C(I) are the central C−C Bonds, and C−C(II) are the four adjacent C−C bonds of pyrene. [b] Relative energy respect to planar pyrene. [c] Experimental bond lengths taken from Reference 49.

ular fragments are bent in two different fashions, one along the direction of the hexagon axes and one along the perpendicular direction, thus reproducing the curvature of the (*n*,0) and (*n*,*n*) nanotubes. To force the molecular models to the same degree of curvature of a given (*n*,0) and (*n*,*n*) nanotube, we kept frozen the Cartesian coordinates of the outer hydrogen atoms of the models along the directions of the C−C bonds bracketing the corresponding subunit in the nanotube. The C−H bond distance was fixed to 1.09 Å, and the same value observed in the correspondent free molecules. Geometry optimizations have then been performed under this constraint. To emphasize the effect of the curvature, we chose to model tubes with quite small diameters, d_t, but still common in synthetic processes,[47] namely, (9,0) and (5,5), with respectively $d_t = 7.05$ and 6.78 Å. To verify the effect of the curvature on the geometrical and electronic structure of our models, we also investigated the electronic structure of the pyrene model with different degrees of curvature, corresponding to tubes with both smaller and larger diameters than the reference (9,0) and (5,5) nanotubes. Moreover, the degree of curvature of the pyrene models can be related to the pyramidalization angle δ on the central C−C bond, according to the definition of Haddon.[48]

Model System for the η^2 Coordination. The pyrene molecule ($C_{16}H_{10}$), formed by the fusion of four hexagonal rings (see Scheme 1), has been examined to investigate the attitude of carbon nanotubes to bind transition metal complexes through the double C≡C bond.

We first performed a geometry optimization on the pyrene molecule ($C_{16}H_{10}$) under D_{2h} symmetry constraints, and indeed, the C−C bond distances show a good agreement with the X-ray structure,[49] with the deviations being only within 0.01 Å (see Table 1). Then we carried out geometry optimizations on the bent-constrained pyrene fragments, as described above, modeling (*n*,0) and (*n*,*n*) nanotubes under C_{2v} symmetry constraints; the results are reported in Table 1. Despite the curvature increase, C−C bonds are substantially unaffected by the bending process for both (*n*,0) and (*n*,*n*) orientations. This result is quite different from that observed for the pyracylene molecule, considered as a model of the fullerene,[37] where a lengthening of the C−C bonds of ca. 0.07 Å upon bending is observed. Indeed, the C−C bond lengthening of the bent-constrained pyrene modeling (5,0) and (3,3) nanotubes, with pyramidalization angles δ respectively equal to 31.8° and 34.8°, close to the value of 37.0° observed for the bent-constrained pyracylene, remains below 0.02 Å, see Table 1. The bending process has a high energetic cost, and a strain energy, E_σ, may be defined for the pyrene model, as the energy increase from the planar structure to the bent-constrained one. It is well-known that by
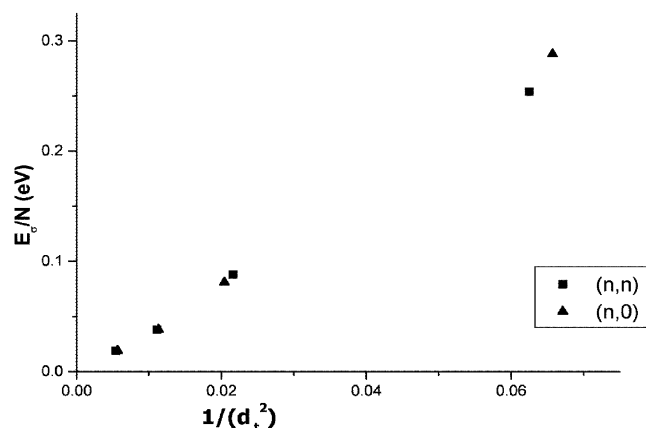
Coordination Chemistry of Carbon Nanotubes

J. Phys. Chem. B, Vol. 106, No. 41, 2002 **10625**

Figure 2. Dependence of the strain energy E_σ/N on the nanotube diameter d_t.

rolling a graphene sheet to form a nanotube the total energy of the system is increased by the strain energy E_σ associated with the curvature of the tube. The strain energy thus increases with decreasing nanotube diameter, so that a nanotube with a small diameter is less stable than a nanotube with a larger diameter. According to the elasticity theory, the strain energy per carbon atom E_σ/N is inversely proportional to the square of the nanotube diameter, d_t:[50]

$$\frac{E_\sigma}{N} = \frac{\sqrt{3}ETd_f^3a^2}{24}\frac{1}{d_t^2} \tag{3}$$

and it is almost of the same magnitude for both $(n,0)$ and (n,n) carbon nanotubes with the same tube diameter.[51] It is interesting to compare the dependence of the strain energy per atom, E_σ/N, calculated for the constrained $(n,0)$ and (n,n) pyrene models, with respect to $(1/d_t)^2$, d_t being the correspondent nanotube diameter, see Table 1. The diagram E_σ/N vs $(1/d_t)^2$ is plotted in Figure 2, and it shows a linear dependence, thus suggesting that the strain energy E increases linearly with increasing the pyramidalization angle δ on the C—C bond of constrained pyrene structures. The diagram also shows that the dependence of the strain energy is essentially the same for both $(n,0)$ and (n,n) models. We can conclude that the strain energy of the bent pyrene models with respect to the planar pyrene reproduces properly the dependence of the strain energy of carbon nanotubes with respect to graphene sheets.

Although it has been recently verified an η^2 coordination of SWNTs sidewalls with the *trans*-IrCl(CO)(PPh$_3$)$_2$ complex,[12] the η^2 interaction on the C—C bond has been investigated with metal–diphosphine fragments M(PR$_3$)$_2$, where R is a phenyl or an ethyl group and M is a metal of the nickel triad. These transition metal complexes indeed are well-known to form stable complexes with electron deficient alkenes[52] and with the fullerene.[53] We performed geometry optimizations on pyrene complexes with M(PH$_3$)$_2$ (M = Ni and Pt), considering an η^2 bonding of the metal fragment with the central C—C bond, with the same parallel orientation observed for metal complexes of olefins[54] and fullerene.[55] To make the calculations feasible, the PR$_3$ ligands were modeled with the smaller PH$_3$ groups. C_{2v} symmetry constraints have been imposed, and the positions of the outer hydrogens have been kept frozen in order to model the $(n,0)$ and (n,n) curvature of the nanotube systems (see Figure 3). As shown in Table 2, complexes of pyrene models for $(9,0)$ and $(5,5)$ nanotubes exihibit quite similar features, with the only significant difference being a slightly higher lengthening (by
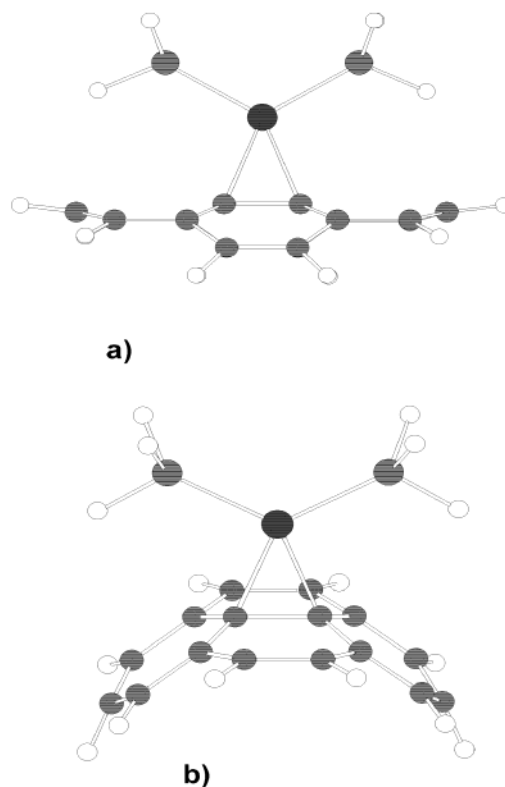

Figure 3. Structures of the $(9,0)$ (a) and $(5,5)$ (b) pyrene complexes with M(PH$_3$)$_2$ (M = Ni and Pt).

TABLE 2: Optimized Geometries of M(PH$_3$)$_2$ (M = Ni and Pt) Complexes with Pyrene Models^a

M(PH$_3$)$_2$	C$_{16}$H$_{10}$	δ	C—C(I)	C—C(II)	M—C
Ni(PH$_3$)$_2$	planar	13.3	1.443	1.446	2.100
Ni(PH$_3$)$_2$	(9,0)	26.4	1.446	1.439	2.031
Ni(PH$_3$)$_2$	(5,5)	29.5	1.485	1.447	2.043
Pt(PH$_3$)$_2$	planar	15.7	1.453	1.450	2.296
Pt(PH$_3$)$_2$	(9,0)	29.1	1.460	1.443	2.170
Pt(PH$_3$)$_2$	(5,5)	30.9	1.505	1.454	2.169

^{a} Bond lengths are given in angstroms, and bond angles are given in degrees. C—C(I) are the central C—C Bonds, and C—C(II) are the four adjacent C—C bonds of pyrene.

TABLE 3: Calculated Bond Dissociation Energies of M(PH$_3$)$_2$ (M = Ni and Pt) Complexes with Pyrene Models (kJ mol^{-1})^a

M(PH$_3$)$_2$	C$_{16}$H$_{10}$	E^*	BSSE	E^b	$E^R_{M(PH_3)_2}$	E^R_{ligand}	D
Ni(PH$_3$)$_2$	planar	113	−41	72	−36	−17	19
Ni(PH$_3$)$_2$	(9,0)	147	−39	108	−37	−15	55
Ni(PH$_3$)$_2$	(5,5)	138	−37	101	−32	−14	55
Pt(PH$_3$)$_2$	planar	110	−5	105	−90	−25	−10
Pt(PH$_3$)$_2$	(9,0)	178	−6	172	−89	−53	30
Pt(PH$_3$)$_2$	(5,5)	169	−6	163	−93	−24	46

^{a} Contributions to the dissociation energy are calculated with basis set I for nickel complexes and basis set II for platinum complexes (see text). ^{b} $E = E^* + $ BSSE.

0.03-0.04 Å) of the central C—C bond for the $(5, 5)$ model. Such results suggest that the metal–ligand interaction is barely affected by the orientation of the honeycomb lattice relative to the axis of the nanotube. Table 2 also shows that the geometric distortion is only slightly higher for platinum than for nickel complexes, with a lengthening of the central C—C bond higher by $0.01-0.02$ Å and a pyramidalization angle higher by $1-3°$ for the Pt(PH$_3$)$_2$ fragment, thus suggesting a slightly stronger interaction of pyrene ligands with the platinum fragment. It is
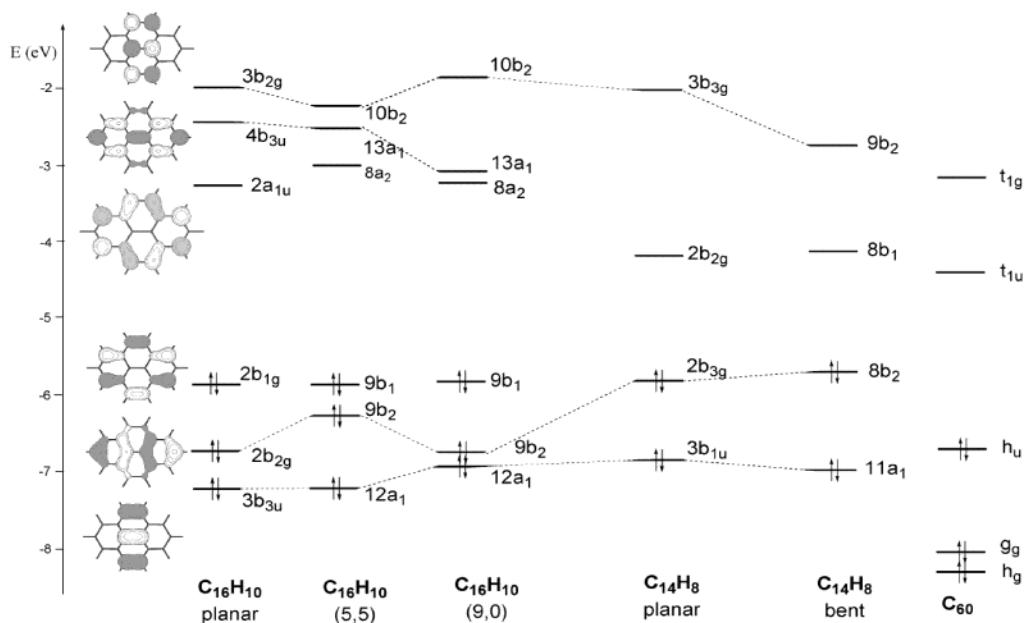
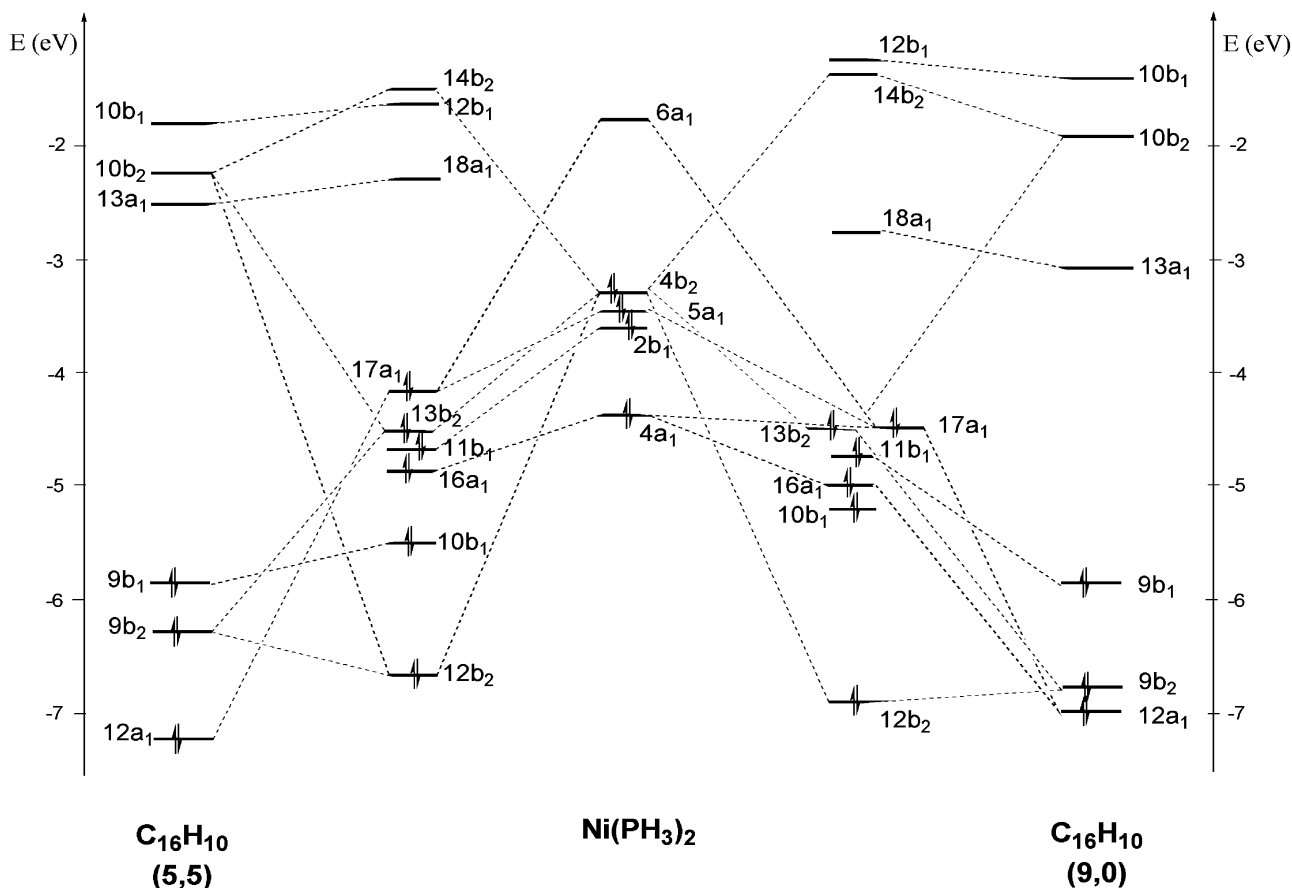**Figure 4.** Frontier orbitals of planar and bent pyrene models compared to orbitals of pyracylene and C_{60}.

Figure 5. MOs correlation diagram for $(PH_3)_2Ni(\eta^2\text{-}C_{16}H_{10})$ complexes for both the (9,0) and (5,5) models.

interesting to compare the geometrical parameters of pyrene complexes with those of pyracylene complexes,[37] that act as good models for C_{60} complexes. The lengthening of the [6,6] C—C bond in the pyracylene unit upon η^2 coordination of a $M(PH_3)_2$ is 0.06—0.15 Å for M = Ni and Pt,[37] significantly higher than the value of 0.03—0.08 Å calculated for constrained pyrene complexes. Moreover, M—C bond distances of pyrene complexes result about 0.02—0.06 Å lower than the values

calculated for pyracylene complexes, thus suggesting a weaker metal—ligand interaction for the pyrene complex.

To estimate the effect of the geometrical constraints on the metal—pyrene bond, geometry optimizations were performed also on the $(PH_3)_2M(C_{16}H_{10})$ complexes without any constraints on the organic moiety. The optimized geometrical parameters suggest that the metal—ligand interaction is weaker than the interaction for constrained models. This is particularly evident

Coordination Chemistry of Carbon Nanotubes

J. Phys. Chem. B, Vol. 106, No. 41, 2002 **10627**

TABLE 4: Mulliken Population of $M(PH_3)_2$ (M = Ni, Pt) Complexes with Pyrene Models[a]

$M(PH_3)_2$	$C_{16}H_{10}$	$M(PH_3)_2$		$C_{16}H_{10}$			
		$6a_1$	$4b_2$	$12a_1$	$13a_1$	$9b_2$	$10b_2$
$Ni(PH_3)_2$	planar	0.07	1.62	1.92	0.08	1.99	0.33
$Ni(PH_3)_2$	(9,0)	0.10	1.57	1.88	0.12	1.99	0.38
$Ni(PH_3)_2$	(5,5)	0.10	1.50	1.91	0.02	1.98	0.43
$Pt(PH_3)_2$	planar	0.26	1.70	1.86	0.05	1.99	0.26
$Pt(PH_3)_2$	(9,0)	0.33	1.58	1.75	0.08	1.99	0.36
$Pt(PH_3)_2$	(5,5)	0.35	1.51	1.84	0.02	1.98	0.40

[a] The values are calculated with basis set I for nickel complexes and basis set II for platinum complexes (see text).

TABLE 5: Bond Dissociation Energy Decomposition of $M(PH_3)_2$ (M = Ni and Pt) Complexes with Pyrene Models (kJ mol^{-1})[a]

$M(PH_3)_2$	$C_{16}H_{10}$	E_{ster}	E_{orb}	E_{A_1}	E_{A_2}	E_{B_1}	E_{B_2}
$Ni(PH_3)_2$	planar	156	−269	−82	−8	−18	−161
$Ni(PH_3)_2$	(9,0)	185	−332	−110	−3	−18	−201
$Ni(PH_3)_2$	(5,5)	192	−330	−74	−6	−18	−231
$Pt(PH_3)_2$	planar	227	−336	−174	−5	−23	−133
$Pt(PH_3)_2$	(9,0)	314	−492	−236	−7	−30	−218
$Pt(PH_3)_2$	(5,5)	328	−498	−209	−7	−30	−251

[a] Contributions to the dissociation energy are calculated with basis set I for nickel complexes and basis set II for platinum complexes (see text).

for $Pt(PH_3)_2$ complexes, where the metal attaching to the (5,5) pyrene model causes a C—C bond lengthening of 0.08 Å with a Pt—C bond distance of 2.169 Å, whereas the unconstrained pyrene complex shows a C—C bond lengthening of 0.03 Å with a Pt—C bond distance of 2.296 Å.

The calculated snapping and bond dissociation energies are reported in Table 3. Inspite of the bond strength order deduced from the geometrical parameters, both the bond dissociation energy D and the snapping energy E are larger for the Ni complexes with respect to the Pt ones. The calculated bond energy terms discussed above for (9,0) and (5,5) pyrene complexes show a comparable bond strength, in agreement with the calculated geometrical parameters. Therefore, the pyrene fragments modeling $(n,0)$ and (n,n) tubes do not show any strong dependence of the interaction energy with a metal fragment on the (n,m) chiral vector. The comparison between these results for the metal complexes of pyrene and those of pyracylene taken from ref 37 show that the bond dissociation energies of pyrene complexes are much smaller than those of the corresponding pyracylene complexes, by 60−70 kJ mol^{-1}. These results clearly suggest that η^2 bonding of metal fragments to nanotubes is much weaker than to fullerene, making questionable the stability of η^2 $M(PH_3)_2$ complexes of carbon nanotubes.

To verify the reliability of the pyrene model, we analyzed the η^2 interaction with $Ni(PH_3)_2$ also on a more extedend fragment, i.e., the $C_{32}H_{14}$ molecule, formed by the fusion of 10 hexagonal rings. Geometry optimizations have been performed on the bent constrained $C_{32}H_{14}$ complexes with $Ni(PH_3)_2$, keeping frozen the position of the outer hydrogens and modeling the (9,0) and (5,5) carbon nanotubes. The geometrical parameters have been found quite close to those of the (9,0) and (5,5) pyrene complexes, with the difference being less than 1%. Moreover, the calculated bond dissociation energies for the (9,0) and the (5,5) $C_{32}H_{14}$ complexes (respectively 73 and 64 kJ mol^{-1}) are quite close to those of the corresponding pyrene complexes, with the difference (10−20 kJ mol^{-1}) being within the intrinsic error bars of the DFT methodology. Therefore, both the geometrical parameters and bonding energies for the $C_{32}H_{14}$ complexes show that pyrene is an adequate cluster model to
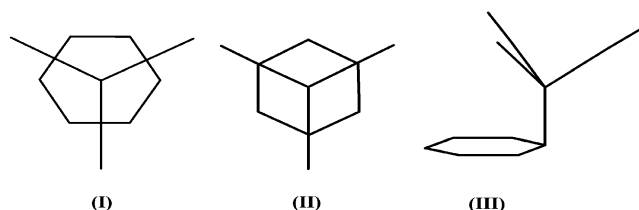
Figure 6. Coordination of the $Cr(CO)_3$ fragment on the hexagonal ring: the hole site configurations in the staggered (**I**) and the eclipsed (**II**) conformation and the atop site (**III**) configuration.

TABLE 6: Optimized Geometries for $Cr(CO)_3$ Complexes with Benzene (Staggered Configuration (I), See Figure 6) and Planar Coronene (Configurations A and B, See Figure 8)[a]

		C—C(I)[b]	C—C(II)[b]	$Cr—C_{ring}$	$Cr—C_{carbonyl}$	C—O
C_6H_6	(**I**)	1.424	1.406	2.218	1.845	1.167
$C_{24}H_{12}$	(**A**)	1.434	1.428	2.308	1.827	1.168
$C_{24}H_{12}$	(**B**)	1.429	1.422	2.273	1.837	1.167

[a] Bond lengths are given in angstroms, and bond angles are given in degrees. [b] CC(I) are C—C bonds *trans* to CO groups, and CC(II) are those in *cis*.

reproduce the essential features of the η^2 bond on the carbon nanotube sidewalls.

The structure and bonding of $M(PH_3)_2$ complexes for the nickel triad can be described in terms of donor−acceptor interactions, according to the Dewar−Chatt−Duncanson model.[56] The σ donation arises from the occupied π MOs of the ligand, whereas the π back-donation occurs through electron donation from the occupied d_π orbitals of the metal to the vacant π^* orbitals of the ligand.

The MOs of the metal fragments have been well characterized in the literature,[57] and those involved in the interaction with the organic fragment are the LUMO of a_1 symmetry with hybrid s−p_z character and two filled b_1 and b_2 orbital with d_π character. The molecular orbitals of pyrene are reported in Figure 4, for both the planar and the (9,0) and (5,5) constrained geometries and compared with those for planar and bent pyracylene and for fullerene. As shown in Figure 4, the HOMO and LUMO of pyrene lack any contribution on the central C—C bond, whereas a π and π^* character has been found in other frontier orbitals. In particular, a π character is shown by the 3rd HOMO $3b_{3u}$, by the 2nd HOMO $2b_{2g}$, and by the 3rd LUMO $3b_{2g}$. Comparing the electronic structure of pyrene and pyracylene,[37] it is evident that the presence of two benzene rings instead of two pentadienyl rings causes a larger HOMO−LUMO gap, thus decreasing the electron affinity of the system and the reactivity toward electron-rich metal fragments. Nevertheless, both pyrene and pyracylene show almost the same energy for the empty orbitals with π^* character, i.e., the 3th LUMO on the pyrene fragment and the 2nd LUMO on the pyracylene. However, the unoccupied π^* C—C orbital of pyrene is not significantly affected by both (9,0)- and (5,5)-like bending, whereas the unoccupied π^* C—C orbital of pyracylene is strongly stabilized by bending to the C_{60}-like curvature. Therefore, although in the presence of pentadienyl rings the pyramidalization process favors the η^2 interactions with transition metal complexes at the [6,6] C—C bonds of fullerene, such an effect is not observed for all-hexagon networks (graphene). Moreover, the polarization of the π electron density is not as efficient as in the pyracylene ligand, because the carbon atoms on the perimeter of the six-membered rings are quite far from the central C—C bond.

As it is shown in Figure 5, the metal−ligand interaction is essentially based on an electron donation from the $12a_1$ orbital,
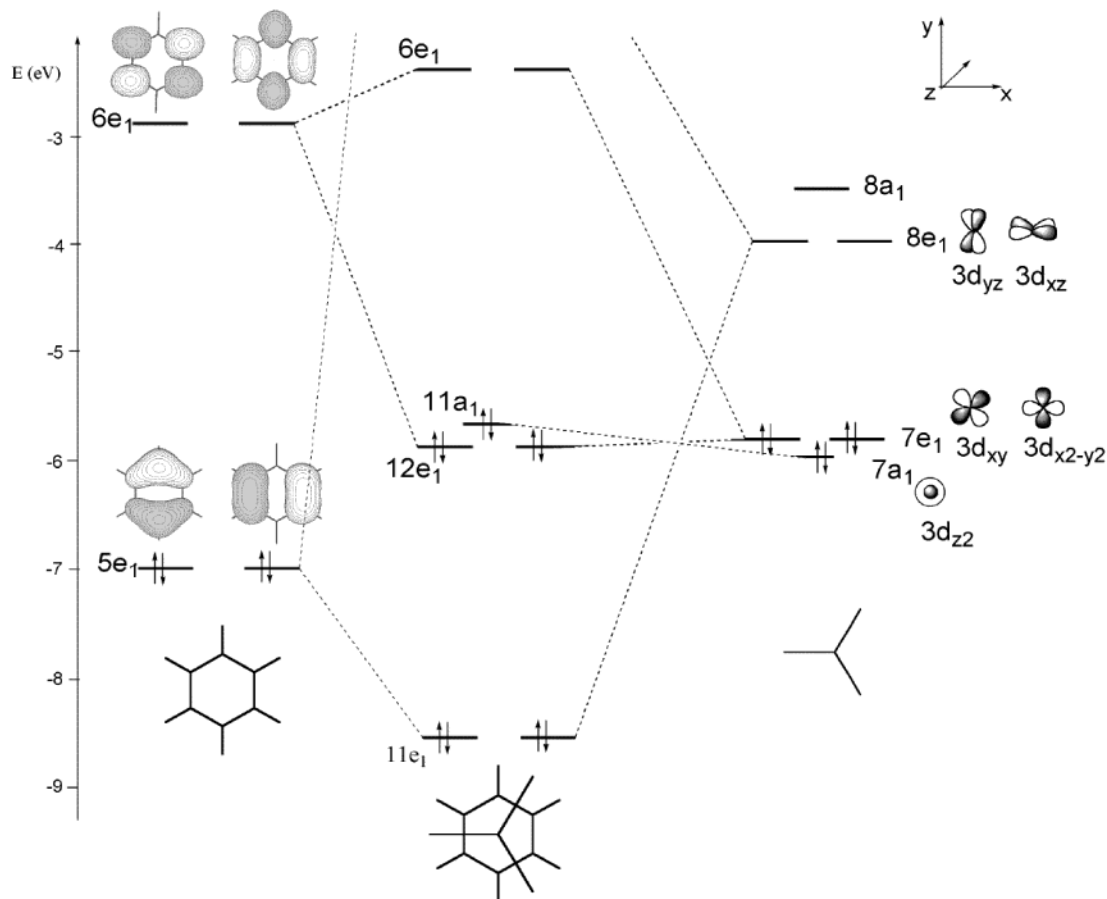
Figure 7. MOs correlation diagram for the Cr(CO)$_3$-(η^6-C$_6$H$_6$) complex in the staggered conformation (**I**).

i.e., the 3rd HOMO of pyrene with π character, to the empty 6a$_1$ orbital of M(PH$_3$)$_2$ and on a π back-donation from the filled d$_\pi$ orbital (4b$_2$) of M(PH$_3$)$_2$ to the 3rd LUMO of pyrene, 10b$_2$, with π^* character. This picture is confirmed by the Mulliken population analysis, reported in Table 4, in terms of the C$_{16}$H$_{10}$ and M(PH$_3$)$_2$ fragments, identifying the orbitals involved in the σ and π back donation. The MO diagram points out that pyrene complexes are somewhat destabilized by the filled-filled interaction between the filled d$_\pi$ orbital, 4b$_2$, and the 2nd HOMO with π^* character. However, both these two MOs are involved as well in the π back-donation interaction essential for the complex stabilization and the four-electron two-orbitals interaction is part of the well characterized metal−ligand interaction of the fullerene complexes.[58] A certain stability of such complexes is preserved, with the four-electrons repulsion being smaller than the σ donation and π back donation.

The results of the energy decomposition for all of the considered pyrene complexes, reported in Table 5, show that the contribution to the orbital interaction term from π back-donation (E_{B2}) dominates over that from σ donation (E_{A1}), as observed for the analogous metal−pyracylene and metal−C$_{60}$ complexes.[37,38] It is worth noting that, although the A$_1$ contribution for the pyrene complex has almost the same value observed for the pyracylene complex (see Reference 37), the B$_2$ contribution is 50−100 kJ mol^{-1} lower, probably as a consequence of the higher energy mismatch between the metal d$_\pi$ and the π^* orbitals in the pyrene molecule, and it is responsible of the weaker metal−pyrene interaction.

Model System for the η^6 Coordination. The coronene molecule (C$_{24}$H$_{12}$) has been employed as a model of a graphene sheet in several issues,[59,60] because it is the smallest PAH having

the essential structural elements of graphite (see Scheme 1). Moreover, coronene showed interesting properties in experiments involving its interaction with metal cations, because it allows multiple coordination sites on the organic surface.[30−36] In this paper, the coronene molecule has been kept frozen in a curved geometry, to model the coordination of Cr(CO)$_3$ on the six-membered ring of SWNTs. Trying to minimize the edge effects typical of finite models, we first set the metal fragment on the central benzene ring of coronene. However, experimental evidences for an η^6-coronene complex with Ru(C$_5$Me$_5$)$^+$ [61] suggest that the most reactive site of coronene is one of the external hexagonal rings, rather than the central one. The reliability of both coordination modes has been verified, comparing the geometries and the bonding energies of the two structures for the planar coronene. For instance, we analyzed in detail the coordination of the Cr(CO)$_3$ metal fragment with the reference benzene compound and with the planar coronene model. Then we performed constrained geometry optimizations on the bent coronene complexes, modeling the (9,0) and (5,5) carbon nanotubes.

Several configurations can be attempted for the Cr(CO)$_3$ coronene complex, setting the metal fragment on the center of the hexagon *(hole site* configuration) in a *staggered* (I) or *eclipsed* (**II**) conformation, or directly above a carbon atom, according to a an *atop site* (**III**) configuration (see Figure 6). The Cr(CO)$_3$ complexes for the reference benzene compound have been characterized in detail both with experiments[16,26] and with theory[17,18] and it is well established that the *hole site* configurations represent the global minimum structures. Our calculations confirm that the η^6 metal−benzene bond manifests almost no barrier to rotation, with the staggered conformation

Coordination Chemistry of Carbon Nanotubes

J. Phys. Chem. B, Vol. 106, No. 41, 2002 **10629**

TABLE 7: Mulliken Population for the Cr(CO)₃ Complexes with Benzene (Staggered Configuration (I), See Figure 6) and Planar Coronene (Configuration A, See Figure 8) with C_{3v} Symmetry Constraints

Cr(CO)₃		C₆H₆ (**I**)		Cr(CO)₃		C₂₄H₁₂ (**A**)			
7e₁	8e₁	5e₁	6e₁	7e₁	8e₁	17e₁	18e₁	19e₁	20e₁
1.67	0.32	1.70	0.30	1.75	0.19	1.83	2.00	0.02	0.21

of benzene complex being only less than 1 kJ mol⁻¹ lower in energy with respect to the eclipsed conformation. This is consistent with the uniform distribution of the electron density and high symmetry of the frontier orbitals of benzene. In the following, we report the results obtained optimizing the Cr(CO)₃ benzene in the lowest staggered conformation and imposing C_{3v} symmetry constraints. The optimized structure shows a C—C bond length alternation, where all of the C—C bonds of the ring *trans* to the carbonyl groups are longer by 0.02 Å respect to those in *cis* (see Table 6). The calculated Cr—C$_{ring}$ bond length is equal to 2.218 Å. The benzene ring maintains the planarity of the carbon framework, whereas all hydrogen atoms are equally tilted toward the metal by 2.2°. The C—C bond alternation on the benzene fragment suggests that the benzene acts as a three ligands donor with respect to the interaction with the Cr(CO)₃ fragment. A comparison of the calculated angles shows that the staggered conformation can be regarded as a "pseudo-octahedral" configuration, with six ligands arranged around the metal atom. The analysis of the electronic structure of the Cr(CO)₃(η^6-C₆H₆) complex shows that the interaction is realized through electron back donation to the π* orbitals of benzene (LUMO, 6e₁) from the occupied orbitals of the metal with δ symmetry, i.e., 7e₁ orbitals (3d$_{x^2-y^2}$ and 3d$_{xy}$), and electron donation from the π orbitals (HOMO, 5e₁) of benzene to the unoccupied orbitals of the metal with π symmetry, i.e., 8e₁ orbitals (3d$_{xz}$ and 3d$_{yz}$) (see Figure 7). The 7a₁ metal orbital (3d$_{z^2}$) belongs to the σ symmetry and does not interact with benzene MOs. According to the C_{3v} symmetry, the δ back donation and the π donation both take place in E_1 symmetry, thus preventing a separation of each contribution to the metal–ligand interaction. Nevertheless, the Mulliken population analysis reported in Table 7 suggests that the two contributions have almost the same importance.

The coordination of Cr(CO)₃ with the planar coronene model reproduces fairly well the features typical of the reference benzene complexes, and our calculations show that the hole site configurations are the lowest in energy also for the coronene complexes. In particular, the staggered conformation results almost isoenergetic with the eclipsed conformation, the difference being less than 1 kJ mol⁻¹, and it will be discussed in the following. We first optimized the Cr(CO)₃ planar coronene complex setting the metal fragment on the central benzene ring and imposing C_{3v} symmetry constraints (see Figure 8A). As it is shown in Table 6, the central benzene ring on the coronene fragment exhibits C—C bond length alternation of 0.01 Å, fairly less than benzene complex (0.02 Å), and the Cr—C$_{ring}$ bond distance lengthens to 2.308 Å. The metal attachment causes a distortion of the hexagonal ring framework, with the external benzene rings being tilted out by 2.5°. The geometrical parameters, both the C—C bond distances and the (carbonyl)– Cr—benzene angles, suggest that the metal atom still accomplishes a "pseudo-octahedral" configuration in the interaction with the planar coronene, analogously to the Cr(CO)₃ benzene complex. However, as it is shown in Table 8, the metal–coronene interaction results weaker than the metal– benzene interaction, by about 100 kJ mol⁻¹, mostly due to the lack of any contributions on the central benzene ring of HOMO

(A)

(B)
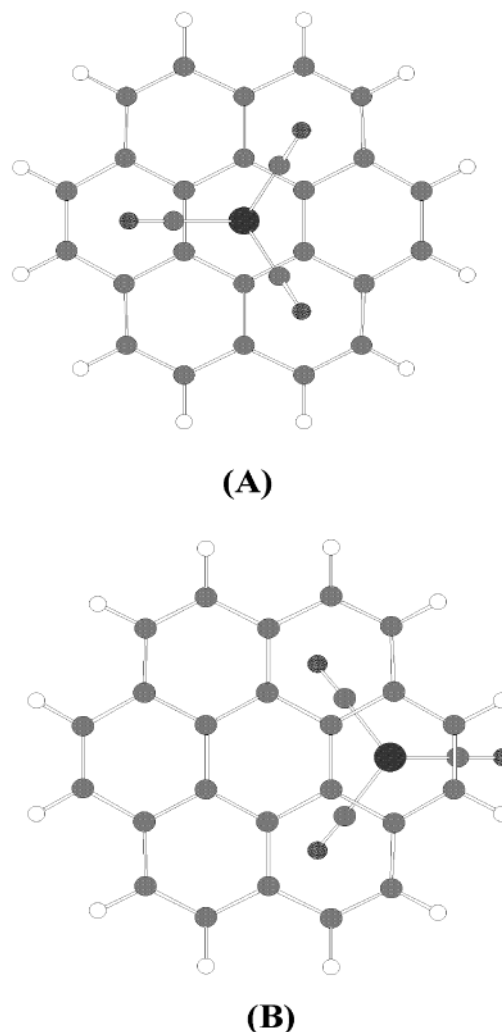
Figure 8. Optimized structures for the planar coronene complexes, setting the Cr(CO)₃ fragment on the central ring (A) and on the external ring (B).

TABLE 8: Calculated Bond Dissociation Energies for Cr(CO)₃ Complexes with Benzene (Staggered Configuration (I), See Figure 6) and Planar Coronene (Configurations A and B, See Figure 8) (kJ mol⁻¹)

		E*	BSSE	E^a	$E^R_{Cr(CO)_3}$	E^R_{Ligand}	D
C₆H₆	(**I**)	267	−37	230	−7	−6	217
C₂₄H₁₂	(**A**)	180	−58	122	−3	−3	116
C₂₄H₁₂	(**B**)	211	−48	163	−5	−5	153

^{a} $E = E + BSSE$.*

and LUMO of coronene. Indeed, the MO analysis shows that the central benzene ring of coronene has a π electron density character on the 2nd HOMO le₁$_g$ and a π* electron density character on the 2nd LUMO 2e₂$_u$, i.e., the former correlates with the HOMO le₁$_g$, the latter with the LUMO 1e₂$_u$ of benzene (see Figure 9). The metal–ligand interaction is still accomplished through an electron back-donation to the 2nd LUMO of coronene from the 7e₁ orbitals of the metal and an electron donation from the 2nd HOMO of coronene to the 8e₁ orbitals of the metal, both the contributions being in E_1 symmetry. The Mulliken population analysis reported in Table 7 supports this pattern, and the bond energy analysis points out that the main contribution to the metal–ligand interaction belongs to the E_1 symmetry (see Table 9). The lower E_1 contribution of coronene complex (−313 kJ mol⁻¹) with respect to the benzene complex
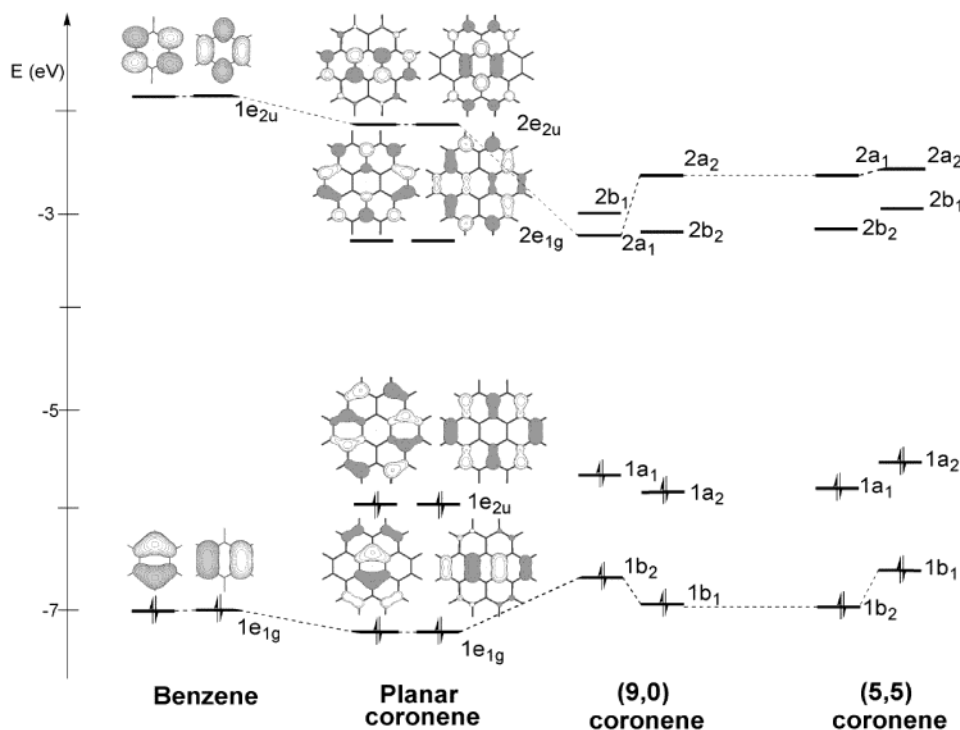
Figure 9. Frontier orbitals of planar and bent coronene models compared to the orbitals of the reference benzene compound.

TABLE 9: Bond Dissociation Energy Decomposition for the Cr(CO)₃ Complexes with Benzene (Staggered Configuration (I), See Figure 6) and Planar Coronene (Configuration A, See Figure 8) with C_{3v} Symmetry Constraints (kJ mol⁻¹)

		E_{ster}	E_{orb}	E_{A_1}	E_{A_2}	E_{E_1}
C_6H_6	(**I**)	255	−522	−88	−2	−450
$C_{24}H_{12}$	(**A**)	216	−396	−79	−3	−313

(−450 kJ mol⁻¹) accounts almost entirely for the weaker metal−ligand bond strength of coronene, and it can be referred to the reduced overlap with the MOs of Cr(CO)₃ caused by the poor localization of the π density on the central benzene ring of coronene.

A geometry optimization has been performed also setting the Cr(CO)₃ fragment at one of the external benzene rings of coronene in a staggered conformation and imposing C_s symmetry constraints, as shown in Figure 8B. The optimized structure B shows a shorter Cr−C_ring bond distance (2.273 vs 2.308 Å) and a higher bond energy term (153 vs 116 kJ mol⁻¹) with respect to the structure A, in agreement with the experimental evidence for the η^6-coronene−Ru(C₅Me₅)⁺ complex, where the coordination site of coronene has been found on the perimetrical benzene rings, rather than on the central ring.[61] Summarizing, our results show that the interaction of the Cr(CO)₃ metal fragment with the planar coronene model accomplishes an η^6 coordination with an external hexagonal ring but with a bond energy lower than that with an isolated benzene molecule.

To reproduce the curvature of (9,0) and (5,5) nanotube systems, constrained geometry optimizations on the Cr(CO)₃ coronene complex have been performed, freeezing the Cartesian coordinates of the hydrogen atoms along the C−C bonds of the corresponding nanotubes. This allows us to outline the effect of the curvature on the metal−ligand interaction, by comparing the planar and the bent-constrained complexes. The metal fragment has been set on the central benzene ring, according to the three configurations illustrated in Figure 6, i.e., the hole site configuration in the staggered (**I**) and eclipsed (**II**) conformation and the atop site configuration (**III**) both for the

(9,0) (see Figure 10) and the (5,5) (see Figure 11) coronene models.

The calculated geometrical parameters reported in Table 10 show that the hole site configurations both for (9,0) and (5,5) complexes provide mostly an η^2 or η^4 rather than an η^6 coordination on the six-membered ring, as observed for benzene and planar coronene complexes. In particular, the (9,0) complex in the staggered conformation (**I**), Figure 10, shows shorter Cr−C bond distances on the C1,C4 (2.193 Å) and on the C2, C3 carbon atoms (2.288 Å); that is, the metal fragment has moved from the center of the hexagon toward the C2−C3 bond. On the other hand, the (9,0) complex in the eclipsed configuration (**II**), Figure 10, shows shorter Cr−C bond distances on the C1 (2.153 Å) and C4 (2.259 Å) carbon atoms, providing mostly an η^2 coordination. Indeed the Cr(CO)₃ fragment has remained on the hexagon axes, moving only sligthly toward the C1 atom and a comparison of the calculated angles points out a "pseudobipyramidal" configuration for the (9,0) eclipsed conformation (**II**), where two carbonyl groups and the Cr−C1 bond lie on the equatorial plane, and the third carbonyl group and the Cr−C4 bond lie on the axial plane (see Figure 12). It is remarkable that this structure shows the shortest Cr−C bond distance among the bent-constrained coronene complex, with Cr−Cl being equal to 2.153 Å, well shorter than the distance calculated for the benzene complex by 0.07 Å. A different situation is found for the (5,5) Cr(CO)₃ complexes in the hole site configurations **I** and **II** (see Figure 11, where the metal coordination essentially refers to an anthracene moiety), which clearly suggests an η^4 coordination to the hexagonal ring, leaving out the two carbon atoms lying on the curved edge of the (5,5) sidewall, i.e., C₁ and C₄. As it is shown in Table 10, the shortest Cr−C bond distances for the staggered **I**(2.231, 2.311 Å) and the eclipsed **II**(2.225, 2.331 Å) conformations have almost the same values, thus suggesting a comparable metal−ligand bond strength for the two conformations.

The stability of the atop site configuration (**III**) has been checked both for (9,0) and (5,5) coronene models (see Figures 10 and 11), and a global minimum was found for the optimized
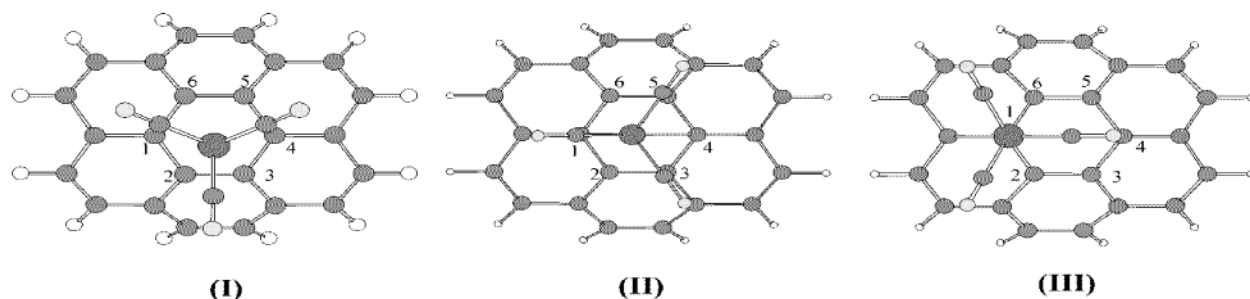
Coordination Chemistry of Carbon Nanotubes

J. Phys. Chem. B, Vol. 106, No. 41, 2002 **10631**

Figure 10. Optimized structures for the (9,0) coronene complexes, setting the $Cr(CO)_3$ fragment on the central ring according to a staggered (**I**), an eclipsed (**II**), and an atop site (**III**) configuration.

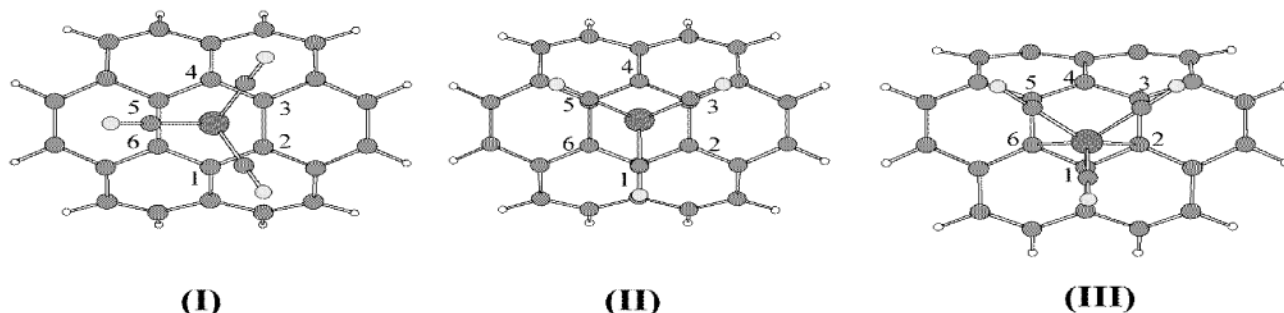**Figure 11.** Optimized structures for the (5,5) coronene complexes, setting the $Cr(CO)_3$ fragment on the central ring according to a staggered (**I**), an eclipsed (**II**), and an atop site (**III**) configuration.

TABLE 10: Calculated Parameters for the $Cr(CO)_3$ Complexes with the Bent-Constrained Coronene Models, According to the Configurations (I), (II), and (III) Shown in Figures 10 and 11[a]

	$C_{24}H_{12}$ (9,0)			$C_{24}H_{12}$ (5,5)		
	(I)	(II)	(III)	(I)	(II)	(III)
C1—C2	1.444	1.444	1.447	1.434	1.429	1.452
C2—C3	1.424	1.422	1.422	1.447	1.446	1.435
C3—C4	1.444	1.434	1.430	1.434	1.435	1.428
C4—C5	1.440	1.434	1.430	1.427	1.435	1.428
C5—C6	1.415	1.422	1.422	1.434	1.446	1.435
C1—C6	1.440	1.444	1.447	1.427	1.429	1.452
Cr—C1	2.193	2.153	2.098	2.453	2.550	2.163
Cr—C2	2.288	2.392	2.796	2.231	2.331	2.372
Cr—C3	2.288	2.425	3.470	2.231	2.225	3.170
Cr—C4	2.193	2.259	3.619	2.453	2.396	3.576
Cr—C5	2.521	2.425	3.470	2.311	2.225	3.170
Cr—C6	2.521	2.392	2.796	2.311	2.331	2.372

[a] Bond lengths are given in angstroms.

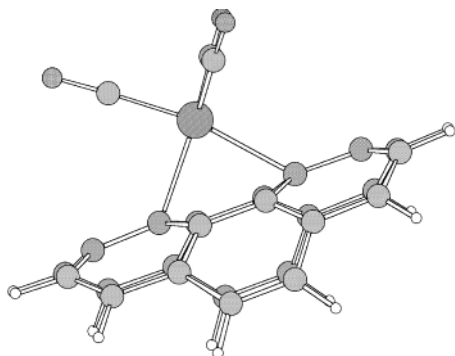**Figure 12.** Pseudobipyramidal configuration for the eclipsed conformation (**II**) of the (9,0) coronene complex with $Cr(CO)_3$.

structures. It is worth noting that, although the (9,0) complex shows the Cr atom directly above the C1 carbon atom, with Cr—C1 equal to 2.098 Å, in the (5,5) complex, the metal moves slightly toward the hexagon center, leading to an almost η^3

TABLE 11: Calculated Bond Dissociation Energies for the $Cr(CO)_3$ Complexes with Bent-Constrained Coronene Models, According to the Configurations (I), (II), and (III) Shown in Figures 10 and 11 (kJ mol⁻¹)

$C_{24}H_{12}$	E*	BSSE	E^a	$E^R_{Cr(CO)_3}$	E^R_{ligand}	D
(9,0) (**I**)	179	−44	135	−3	−10	122
(9,0) (**II**)	175	−44	131	−5	−9	117
(9,0) (**III**)	128	−32	96	−3	−5	88
(5,5) (**I**)	171	−44	127	−3	−7	117
(5,5) (**II**)	177	−42	135	−3	−9	123
(5,5) (**III**)	133	−36	97	−8	−5	84

[a] E = E* + BSSE.

coordination with the three carbon atoms C1, C2, and C6 (Cr—C1 = 2.163 Å and Cr—C2 = Cr—C6 = 2.372 Å).

The bond energy analysis reported in Table 11 shows that the hole site configurations **I** and **II**, allowing an η^2 or η^4 coordination for the metal, are more stable than the atop site configuration by about 30-40 kJ mol⁻¹.

It is worth noting that, inspite of planar and (9,0) coronene complexes, the (5,5) coronene complexes are more stable in the eclipsed conformation (**II**) rather than in the staggered conformation (**I**) by 7 kJ mol⁻¹.

An MO analysis for the (9,0) and (5,5) bent coronene complexes shows that the poor localization of the π density on the central benzene ring makes the metal—ligand interaction almost unaffected by the bending process. As result of coronene bending, we observe a slight destabilization of the second HOMO, $1e_{1g}$, and a slight stabilization of the second LUMO, $2e_{2u}$, of the planar coronene, except for the second LUMO of the (9,0) model, that results strongly stabilized by 1 eV (see Figure 9).

Our investigations prove that the bending process enforces a different coordination on the curved coronene systems, modeling the nanotubes sidewalls, with respect to the planar systems, as a consequence of the loss of planar aromaticity. The optimized geometries show that the chromium arranges an η^2 or an η^4 coordination with the nearest carbon atoms on the hexagonal

10632 *J. Phys. Chem. B, Vol. 106, No. 41, 2002*

Nunzi et al.

ring of bent constrained coronenes, modeling carbon nanotubes, rather than an η^6 coordination as in the planar models, modeling graphene sheets.

Conclusions

In this paper, we investigated the interactions of carbon nanotubes with transition metal complexes by means of a cluster model approach and the DFT. The chemical reactivity on carbon nanotubes is intrinsically connected to the curvature of the system, i.e., to the (*n,m*) parameters. The rolling up of the graphene sheet to form the tube causes a rehybridization of carbon bonding orbitals (nonplanar sp^2 configuration), thus leading to a splaying-out of the π density of the graphene sheet, whose magnitude is related to the diameter of the tube. This forces us to perform constrained geometry optimizations on planar aromatic hydrocarbons as models, freezing the hydrogen positions along the directions of the C—C bonds.

The pyrene molecule (C$_{16}$H$_{10}$) has been used to model the η^2 interaction of a C—C bond of SWNTs with M(PH$_3$)$_2$ (M = Ni and Pt). The molecular model approach for the characterization of the η^2 bond fashion on the carbon nanotubes and on the fullerene respectively through the pyrene and pyracylene systems suggests that η^2 bonding of metal fragments to nanotubes is much weaker than to fullerene, making questionable the stability of η^2 M(PH$_3$)$_2$ complexes of carbon nanotubes. Both geometrical parameters and bonding energies for the (PH$_3$)$_2$M(C$_{16}$H$_{10}$) (M = Ni and Pt) show that the metal–ligand interaction is much weaker in the pyrene models of SWNTs than in the pyracylene model of fullerene. Moreover, the η^2 metal interaction with (9,0) and (5,5) bent-constrained pyrene models does not show any dependence on the (*n,m*) chiral vector.

The coronene molecule (C$_{24}$H$_{12}$) has been adopted to analyze the η^6 interaction of SWNTs with the Cr(CO)$_3$ fragment. The coordination site of coronene has been found on the external rings, where the terminal effects because of the limit of the model are relevant, rather than on the central ring, which represents a more suited site to model the hexagonal ring of SWNTs. Nevertheless, the characterization of the coronene complexes gives us useful information about the coordination of chromium-tricarbonyls on the SWNTs sidewalls. Our calculations point out that, although planar aromatic systems arrange an η^6 coordination for the chromium atom, curved π systems prefer an η^2 or η^4 coordination. Moreover, we found that the (9,0) coronene model with the Cr(CO)$_3$ fragment in an eclipsed conformation has an unusual bipyramidal configuration, thus suggesting the possibility of a new metal coordination on the sidewall of (*n,*0) nanotubes and providing the basis for further investigations on these systems. It is worth noting that theoretical investigations on the interaction of carbon nanotubes with transition metals really represent an innovative approach toward the functionalization of SWNTs, pointing out the most favorite coordination sites on the sidewalls and the effects of the metal–nanotube bond on the electronic structure of the system.

References and Notes

(1) Iijima, S.; Ichihashi, T. *Nature (London)* **1992**, *363*, 603.

(2) Saito, S. *Science* **1997**, *278*, 77.

(3) Dresselhaus, M. S.; Dresselhaus, G.; Eklund, P. C. *Science of Fullerenes and Carbon Nanotubes*; Academic Press: New York, 1996.

(4) Falvo, M. R.; Clary, G. J.; Taylor, R. M. I.; Chi, V.; Brooks, F. P.; Washburn, S.; Superfine, R. *Nature* **1997**, *389*, 582.

(5) Odom, T. W.; Huang, J. L.; Kim, P.; Lieber, C. M. *Nature* **1998**, *392*, 62.

(6) Braga, D.; Grepioni, F.; Desiraju, G. R. *Chem. Rev.* **1998**, *98*, 1375.

(7) Mickelson, E. T.; Huffman, C. B.; Rinzler, A. G.; Smalley, R. E.; Hauge, R. H.; Margrave, J. L. *Chem. Phys. Lett.* **1998**, *296*, 188.

(8) Boul, P. J.; Liu, J.; Mickelson, E. T.; Huffman, C. B.; Ericson, L. M.; Chiang, I. W.; Smith, K. A.; Colbert, D. T.; Hauge, R. H.; Margrave, J. L.; Smalley, R. E. *Chem. Phys. Lett.* **1999**, *310*, 367.

(9) Chen, J.; Hamon, M. A.; Hu, H.; Chen, Y.; Rao, A. M.; Eklund, P. C.; Haddon, R. C. *Science* **1998**, *282*, 95.

(10) Koshio, A.; Yudasaka, M.; Zhang, M.; Iijima, S. *Nano Lett.* **2001**, *1*, 361.

(11) Chen, R. J.; Zhang, Y.; Wang, D.; Dai, H. *J. Am. Chem. Soc.* **2001**, *123*, 3838.

(12) Banerjee, S.; Wong, S. S. *Nano Lett.* **2002**, *2*, 49.

(13) Dagani, R. *Chem. Eng. News* **1999**, *77*(2), 31.

(14) Muetterties, E. L.; Bleeke, J. R.; Wucherer, E. J.; Albright, T. A. *Chem. Rev.* **1982**, *82*, 499.

(15) Siebert, W.; Wilke, G. *J. Organomet. Chem.* **2002**, *641*, 1. Köcher, S.; Lang, H. *J. Organomet. Chem.* **2002**, *641*, 62. Oprunenko, Y.; Malyugina, S.; Vasil'ko, A.; Lyssenko, K.; Elschenbroich, C.; Harms, K. *J. Organomet. Chem.* **2002**, *641*, 208.

(16) Kukolich, S. G. *J. Am. Chem. Soc.* **1995**, *117*, 5512.

(17) Elian, M.; Chen, M. M. L.; Mingos, D. M. P.; Hoffmann, R. *Inorg. Chem.* **1976**, *15*, 1148.

(18) Suresh, C. H.; Koga, N.; Gadre, S. R. *Organometallics* **2000**, *19*, 3008.

(19) Monovich, L. G.; LeHuerou, Y.; Ronn, M.; Molander, G. A. *J. Am. Chem. Soc.* **2000**, *122*, 52.

(20) Hörstermann, D.; Schmalz, H.-G.; Kociok-Khon, G. *Tetrahedron* **1999**, *55*, 6905.

(21) Tanaka, T.; Mikamiyama, H.; Maeda, K.; Itawa, C.; In, Y.; Isada, T. J. Org. Chem. **1998**, *63*, 9782.

(22) Gibson (née Thomas), S. E.; Reddington, E. G. A. *Chem. Commun.* **2000**, 989.

(23) Solladié-Cavallo, A. In *Advances in Metal-Organic Chemistry*; Liebeskind, L. S., Ed.; JAI Press: Stamford, CT, 1991; Vol. 2, pp 231.

(24) Uemura, M. In *Advances in Metal-Organic Chemistry*; Liebeskind, L. S., Ed.; JAI Press: Stamford, CT, 1991; Vol. 2, pp 231.

(25) Gibson (née Thomas), S. E.; Saladin, S. A.; Sur, S. *Chem. Commun.* **2000**, 2011.

(26) Li, J.; Hunter, A. D.; McDonald, R.; Santarsiero, B. D.; Bott, S. G.; Atwood, J. L. *Organometallics* **1992**, *11*, 3050 and references therein.

(27) Aihara, J. *J. Phys. Chem.* **1994**, *98*, 9773.

(28) Mintmire, J. W.; Dunlap, B. I.; White, C. T. *Phys. Rev. Lett.* **1992**, *68*, 631.

(29) Blase, X.; Benedict, X. L.; Shirley, E. L.; Louie, S. G. *Phys. Rev. Lett.* **1994**, *72*, 1878.

(30) Pozniak, B. P.; Dunbar, R. C. *J. Am. Chem. Soc.* **1997**, *119*, 10439.

(31) Buchanan, J. W.; Reddic, J. E.; Grieves, G. A.; Duncan, M. A. *J. Phys. Chem. A* **1998**, *102*, 6390.

(32) Buchanan, J. W.; Grieves, G. A.; Reddic, J. E.; Duncan, M. A. *Int. J. Mass Spectrom.* **1999**, *182/183*, 323.

(33) Buchanan, J. W.; Grieves, G. A.; Flynn, N. D.; Duncan, M. A. *Int. J. Mass Spectrom.* **1999**, *185–187*, 617.

(34) Foster, N. R.; Grieves, G. A.; Buchanan, J. W.; Flynn, N. D.; Duncan, M. A. *Chem. Phys. Lett.* **2001**, *341*, 376.

(35) Duncan, M. A.; Knight, A. M.; Negishi, Y.; Nagao, S.; Nakamura, Y.; Kato, A.; Nakajima, A.; Kaya, K. *Chem. Phys. Lett.* **1999**, *309*, 49.

(36) Duncan, M. A.; Knight, A. M.; Negishi, Y.; Nagao, S.; Judai, K.; Nakajima, A.; Kaya, K. *J. Phys. Chem. A* **2001**, *105*, 10093.

(37) Nunzi, F.; Sgamellotti, A.; Re, N. *J. Chem. Soc., Dalton Trans.* **2002**, 399.

(38) Nunzi, F.; Sgamellotti, A.; Re, N. *Organometallics* **2000**, *19*, 1628.

(39) Baerends, E. J.; Ellis, D. E.; Ros, P. *Chem. Phys.* **1973**, *2*, 41. Boerrigter, P. M.; Velde, G.; Baerends, E. J. *Int. J. Quantum Chem.* **1988**, *33*, 87.

(40) Rosa, A.; Ehlers, A. W.; Baerends, E. J.; Snijders, J. G.; te Velde, G. *J. Phys. Chem.* **1996**, *100*, 5690.

(41) Vosko, S. H.; Wilk, L.; Nusair, M. *Can. J. Phys.* **1980**, *58*, 1200.

(42) Becke, A. D. *Phys. Rev.* **1988**, *A38*, 2398.

(43) Perdew, J. P. *Phys. Rev.* **1986**, *B33*, 8822.

(44) Ziegler, T.; Tshinke, V.; Baerends, E. J.; Snijders, J. G.; Ravenek, W. *J. Phys. Chem.* **1989**, *93*, 3050.

(45) (a) Boerrigter, P. M. Spectroscopy and bonding of heavy element compounds Ph.D. Thesis, Vrije University, 1987; (b) Li, J.; Schreckenbach, G.; Ziegler, T. *J. Am. Chem. Soc.* **1995**, *117*, 486.

(46) Boys, S. F.; Bernardi, F. *Mol. Phys.* **1970**, *19*, 553.

(47) Nikolaev, P.; Bronikowski, M. J.; Bradley, R. K.; Rohmund, F.; Colbert, D. T.; Smith, K. A.; Smalley, R. E. *Chem. Phys. Lett.* **1999**, *313*, 91.

(48) Haddon, R. C. *Science* **1993**, *261*, 1545.

Coordination Chemistry of Carbon Nanotubes

J. Phys. Chem. B, Vol. 106, No. 41, 2002 **10633**

(49) Dixon, D. A.; Kleier, D. A.; Lipscomb, W. *N. J. Am. Chem. Soc.* **1978**, *100*, 5681.

(50) Tibbetts, G. G. *Appl. Phys. Lett.* **1983**, *42*, 666.

(51) Mintmire, J. W.; White, C. T. *Carbon* **1995**, *33*, 893.

(52) Ittel, S. D.; Ibers, J. A. *Adv. Organomet. Chem.* **1976**, *14*, 33. Hartley, F. R. In *Comprehensive Organometallic Chemistry*; Wilkinson, G., Ed.; Pergamon: London, 1982; Vol. 6, pp 471. Young B. G. In *Comprehensive Organometallic Chemistry II*; Abel, E. W., Stone, F. G. A., Wilkinson, G., Eds.; Pergamon: London, 1995; Vol. 9, p 533.

(53) (a) Fagan, P. J.; Calabrese, J. C.; Malone, B. *Science* **1991**, *252*, 1160. (b) Bashilov, V. V.; Petrovskii, P. V.; Sokolov, V. I.; Lindeman, S. V.; Guzey, I. A.; Struchkov, Y. T. *Organometallics* **1993**, *12*, 991. (c) Nagashima, H.; Yamaguchi, H.; Kato, Y.; Saito, Y.; Haga, M.; Itoh, K. *Chem. Lett.* **1993**, 2153.

(54) (a) Cheng, P. T.; Nyburg, S. C. *Can. J. Chem.* **1972**, *50*, 912. (b) Guggenberger, L. J. *Inorg. Chem.* **1973**, *12*, 499.

(55) Balch, A. L.; Olmstead, M. M. *Chem. Rev.* **1998**, *98*, 2123.

(56) Dewar, M. J. S. *Bull. Soc. Chim. (Fr.)* **1951**, *18*, C71. Chatt, J.; Ducanson, L. A. *J. Chem. Soc.* **1953**, 2939.

(57) Albright, T. A.; Burdett, J. K.; Whangbo, M. H. *Orbital Interactions in Chemistry*; Wiley: New York, 1985.

(58) Lopez, J. A.; Mealli, C. *J. Organomet. Chem.* **1994**, *478*, 161.

(59) Ruuska, H.; Pakkanen, T. A. *J. Phys. Chem. B* **2001**, *105*, 9541.

(60) Jeloaica, L.; Sidis, V. *Chem. Phys. Lett.* **1999**, *300*, 157 and references therein.

(61) Chavez, I.; Cisternas, A.; Otero, M.; Romin, E. Z. *Naturforsch.* **1990**, *45*(5), 658.